Host lipidome analysis during rhinovirus replication in human bronchial epithelial cells identifies potential therapeutic targets

An Nguyen[1], Anabel Guedán[2,3], Aurelie Mousnier[2,4], Dawid Swieboda[2], Qifeng Zhang[1], Dorottya Horkai[1], Nicolas Le Novere[1], Roberto Solari[2] & Michael J. O. Wakelam[1*]

[1]Babraham Institute, Babraham Research Campus, Cambridge CB22 3AT, UK [2]MRC & Asthma UK Centre in Allergic Mechanisms of Asthma, Airway Disease Infection Section, National Heart and Lung Institute, Imperial College, Norfolk Place, London W2 1PG, UK [3]Current address: The Francis Crick Institute, 1 Midland Road, London NW1 1AT. [4]Current address: Centre for Experimental Medicine, School of Medicine Dentistry & Biomedical Sciences, Queen's University Belfast, Medical Biology Centre, 97 Lisburn Road, Belfast BT9 7BL, Northern Ireland

*Correspondence: Michael.wakelam@babraham.ac.uk

Running title: Lipidomics identifies therapeutic targets

ABSTRACT

In patients with asthma or chronic obstructive pulmonary disease rhinovirus infections can provoke acute worsening of disease and limited treatment options exist. Viral replication in the host cell induces significant remodeling of intracellular membranes, but few studies have explored this mechanistically or as a therapeutic opportunity. We performed unbiased lipidomic analysis on human bronchial epithelial cells infected over a 6 hour period with the RV-A1b strain of rhinovirus to determine changes in 493 distinct lipid species. Through pathway and network analysis we identified temporal changes in the apparent activities of a number of lipid metabolizing and signaling enzymes. In particular, analysis highlighted fatty acid synthesis and ceramide metabolism as potential anti-rhinoviral targets. To validate the importance of these enzymes in viral replication, we explored the effects of commercially-available enzyme inhibitors upon RV-A1b infection and replication. Ceranib-1, D609 and C75 were the most potent inhibitors, which confirmed that fatty acid synthase and ceramidase are potential inhibitory targets in rhinoviral infections. More broadly, this study demonstrates the potential of lipidomics and pathway analysis to identify novel targets to treat human disorders.

Keywords: lipidomics, rhinovirus, human brochial epithelial cells

Introduction

Rhinoviruses (RVs), members of the picornavirus family are the causative agent of the common cold. Like other picornaviruses they have a single positive-strand RNA genome of about 7.5kb. Following infection and entry into the cytoplasm, the viral genome is translated and post-translationally cleaved into 4 capsid proteins and 7 non-structural proteins that participate in viral replication. All known picornaviruses use the cytoplasmic surface of ER/Golgi membranes for genome replication and the morphology of these membranes is greatly remodeled by the virus into replication organelles or complexes. The viral non-structural proteins 2B, 2C and 3A associate with the ER and Golgi membranes and are thought important in remodeling through recruitment of host proteins. In addition to morphological changes to the ER and Golgi, viral replication induces changes to the lipid composition of cellular membranes. A number of host factors have been identified as being involved in membrane remodeling and viral replication including Golgi Brefeldin A Resistant Guanine Nucleotide Exchange Factor 1/ ADP-ribosylation factor 1 (GBF1/Arf1) (1), phosphatidylinositol-4-kinase (PI4K) (2, 3), Oxysterol Binding Protein (OSBP) (4-6) and Protein Kinase D (PKD) (7), inhibitors of these targets inhibit replication of a number of picornaviruses. This suggests membrane remodeling is important for picornaviral replication and represents potential for the discovery of novel anti-viral targets.

In this study we have performed an open platform unbiased analysis of changes to the host lipidome during a single replicative cycle of RV in primary human bronchial epithelial cells (HBECs). We analyzed lipid samples extracted from synchronously infected cells over a time course of 6 hours and found evidence of multiple lipid metabolic pathways being altered with an unexpected and remarkable complexity of changes in both lipid class and the length and saturation of acyl chains. These studies identified lipid modifying enzymes as potential anti-viral targets and we tested these with chemical inhibitors demonstrating particular lipid modifying enzymes may represent potential anti-viral drug targets.

3

MATERIAL & METHODS

Cells:

Human bronchial epithelial cells (HBECs) (CC2540; Lonza) were cultured following manufacturer's recommendations. HeLa H1 (ATCC CRL-1958) and HeLa Ohio (European Collection of Authenticated Cell Cultures [ECACC] 930021013) were used to produce RV1B and to perform viral endpoint titre determination, respectively.

Virus infections:

HRV-A1b stocks (ATCC) were produced by infection of HeLa H1 and were titrated on HeLa Ohio cells to determine the $TCID_{50}$/mL.

A number of compounds were tested for their anti-viral effect at a single concentration of 10µM. Compounds showing activity were subsequently tested for their anti-viral activity over concentration-response curves ranging from 0.5 to 20µM. For the single dose experiments, a dose at which highest virus replication inhibition is achieved without cytotoxicity was used (10µM for Ceranib 1 and D609; 20µM for 3-O-Methyl-SM, SK-I, SK-II, VU 0155069 and C75). HBECs were pre-treated with the specified concentration of the compounds or the vehicle alone for 1h at 37°C. RV-A1b was added to the cells at MOI 5; incubated for 1h at room temperature (RT) to obtain a synchronous infection, washed with BEBM to remove unbound virus; and further incubated in fresh medium containing the compound or the vehicle for 7h at 37°C. At the end of the infection/replication period, cells were harvested for further analysis by qRT-PCR, WB or endpoint titre determination by $TCID_{50}$. The cytotoxicity of the compounds at 9h was determined by using the Viral ToxGlo assay (Promega) according to the manufacturer's instructions.

qRT-PCR:

4

After the 7h incubation period, cells were lysed with RLT buffer (Qiagen) supplemented with β-Mercaptoethanol (Sigma) at 1:200 dilution. mRNA was extracted by using the RNeasy minikit (Qiagen) according to manufacturer´s instructions. 1µg of RNA was reverse-transcribed for cDNA synthesis for 1h at 37°C by using the Omniscript RT kit (Qiagen). Quantification of the levels of viral RNA was conducted by using specific primer (Invitrogen) and probe (Eurofins) sequences, as follows: RV forward primer 5´-GTGAAGAGCCSCRTGTGCT-3´ (50 nM), RV reverse primer 5´-GCTSCAGGGTTAAGGTTAGCC-3´ (300 nM), HRV probe 5´-TGAGTCCTCCGGCCCCTGAATG-3´ (100 nM); 18S forward primer 5´-CGCCGCTAGAGGTGAAATTCT-3´ (300 nM), 18S reverse primer 5´-CATTCTTGGCAAATGCTTTCG-3´ (300 nM), and 18S probe 5´-ACCGGCGCAAGACGGACCAGA-3´ (100 nM). Analysis was performed by using QuantiTect Probe PCR master mix (Qiagen) and the LightCycler 480 real-time PCR system (Roche). For absolute quantification, the level of each gene was normalized to the level of 18S rRNA, and the exact number of copies of the gene of interest was calculated by using a standard curve generated by the amplification of plasmid DNA.

Western Blotting:

Cells were lysed in ice-cold radioimmunoprecipitation assay (RIPA) buffer (Sigma) supplemented with protease (Roche) and phosphatase (Sigma) inhibitors (according to the manufacturers' instructions), and their protein content was measured by the bicinchoninic acid assay (Thermo Scientific). Equal amounts of protein were loaded onto 4 to 12% Bis-Tris SDS-PAGE gels (Life Technologies), followed by transfer onto polyvinylidene difluoride (PVDF) membranes (Life Technologies). Membranes were blocked in Tris-buffered saline (TBS) supplemented with 5% bovine serum albumin (BSA) and 0.1% Tween 20 for 1h at RT. Primary antibodies were incubated overnight at 4°C, and secondary antibodies were incubated for 1h at RT, followed by the addition of ECL reagent and data collection on a Fusion FX7 image analyser (Vilber Lourmat). Analysis of quantified images was performed by using ImageJ. Primary and secondary antibodies used: rabbit anti-RV 2C (generated and used as previously described

(8)), rabbit anti-Lamin B1 (LB1) (Proteintech), donkey anti-rabbit conjugated to horseradish peroxidase (HRP) (Jackson ImmunoResearch).

LDL uptake:

HBECs were grown on coverslips and pre-treated with vehicle or compound for 1h at 37°C. Human non-acetylated LDL conjugated to BODIPY™ FL (Thermo Fisher Scientific) was added at a final concentration of 25µg/mL, also in the presence of vehicle or compound, and cells were incubated for 1h at 37°C. Cells were fixed with 4% paraformaldehyde (PFA), washed with PBS, permeabilized then stained with a mouse anti-GM130 antibody (BD Pharmigen) followed by a donkey anti-mouse antibody coupled to Alexa Fluor 546 (Jackson ImmunoResearch). LDL quantification is shown as the fluorescence ratio between LDL and GM130. Cells from five different fields of each condition and from three independent experiments were quantified using ImageJ.

Virus endpoint titre determination (TCID$_{50}$/mL):

Cells and supernatant were scraped, frozen-thawed twice, and centrifuged at 10,000g for 5 min at 4°C to remove cell debris, and the supernatant containing the viral particles was used to perform TCID$_{50}$ titration assays, as follows. HeLa Ohio cells were incubated in 96-well plates in DMEM (supplemented with 2% FBS and 1% penicillin-streptomycin) with 8-fold dilutions of the virus in six replicates for 5 days. Titration was assessed by the presence or absence of cytopathic effect (CPE) in each well by using an RV-A1B stock as a positive control.

Lipidomics

Cells were harvested, washed twice in ice-cold PBS and then flash-frozen in liquid nitrogen. Cell pellets were washed twice with cold PBS and re-suspended in 1.5 ml methanol and 40 µl lipid standards added. This sample of lipid standard contained 17 : 0-cholesterol ester (CE; 400 ng), cholesterol-d7 (CH-d7; 1000 ng), 17 : 1/17 : 1/17 : 1-triacylglycerol (TG; 800 ng), 17 : 0/18 : 1-

6

diacylglycerol (DG; 200 ng), 17 : 0-monoacylglycerol (MG; 100 ng), 17 : 0-free fatty acid (FFA; 400 ng), 17 : 0-fatty acyl coenzyme A (FaCoA; 100 ng), 17 : 0-fatty acyl carnitine (FaCN; 50 ng), 17 : 0/18 : 1-phosphatidic acid (PA; 50 ng), 17 : 0/18 : 1-phosphatidylcholine (PC; 400 ng), 17 : 0/18 : 1-phosphatidylethanolamine (PE; 200 ng), 17 : 0/18 : 1-phosphatidylglycerol (PG; 50 ng), 17 : 0/20 : 4-phosphatidylinositol (PI; 400 ng), 17 : 0/18 : 1-phosphatidylserine (PS; 200 ng), 14 : 0/14 : 0/14 : 0/14 : 0-cardiolipin (CL; 200 ng), C17-platelet-activating factor (PAF; 50 ng), C17-2-lysoplatelet-activating factor (LysoPAF; 50 ng), 17 : 0-2-lysophosphatidic acid (LPA; 50 ng), 17 : 0-2-lysophosphatidylcholine (LPC; 100 ng), 17 : 1-2-lysophosphatidylethanolamine (LPE; 100 ng), 17 : 12-lysophosphatidylglycerol (LPG; 50 ng), 17 : 1-2-lysophosphatidylinositol (LPI; 100 ng), 17 : 1-2-lysophosphatidylserine (LPS; 50 ng), C17-ceramide (Cer; 50 ng), C17-sphingosine (SG; 50 ng), 12 : 0-ceramide-1-phosphate (Cer1P; 50 ng), C17-sphingosine-1-phosphate (S1P; 50 ng), C17-sphingomyelin (SM; 400 ng), C17-sphingosine-1-phosphocholine (S1P; 50 ng) and C17-monosulfogalatosyl ceramide (Sul-Gal-Cer; 50 ng). 1.5 ml of LCMS-grade water and 3 ml chloroform were added. The mixture was subjected to Folch extraction. After collection of the lower phase, the upper phase was re-extracted with 3 ml synthetic lower phase (chloroform/methanol/water at volume ratio of 2:1:1, using the lower phase for re-extraction of lipid). The lower phase from both extractions was combined and dried under vacuum at 20 °C with SpeedVac (Thermo) and re-dissolved in 100 µl chloroform. 7 µl were injected for LC/MS/MS analysis. A Thermo Orbitrap Elite system (Thermo Fisher) hyphenated with a five-channel online degasser, four-pump, column oven, and autosampler with cooler Shimadzu Prominence HPLC system (Shimadzu) was used for lipid analysis as previously described (9, 10). In detail, lipid classes were separated on a normal-phase Cogent silica-C column (150 × 2.1 mm, 4 µm, 100 Å, MicoSolv Technology) with hexane/dichloromethane/chloroform/methanol/acetanitrile/ water/ethylamine solvent gradient based on the polarity of head group. High resolution (240k at m/z 400) / accurate mass (with mass accuracy <5 ppm) were used for molecular species identification and quantification. The identity of lipid was further confirmed by reference to appropriate lipids standards. Orbitrap Elite

mass spectrometer operation conditions were as follows. For positive ion analysis: heated ESI source in positive ESI mode; heater temperature, 325 °C; sheath gas flow rate (arb), 35; aux gas flow rate (arb), 5; sweep gas flow rate (arb), 0; I spray voltage, 3.5 kV; capillary temperature, 325 °C; and S-lens RF level, 60%. Orbitrap mass analyzer was operated as SIM scan mode with two events. Event 1: mass range, m/z 238-663; and mass resolution, 240 k at m/z 400. Event 2: mass range, m/z 663-1088; and mass resolution, 240 k at m/z 400. B. For negative ion analysis, heated ESI source in negative ESI mode; heater temperature, 325 °C; sheath gas flow rate (arb), 45; aux gas flow rate (arb), 10; sweep gas flow rate (arb), 0; I spray voltage, 3.0 kV; capillary temperature, 375 °C; and S-lens RF Level, 70%. Orbitrap mass analyzer was operated as SIM scan mode with two events. Event 1: mass range, m/z 218-628; and mass resolution, 240 k at m/z 400. Event 2: mass range, m/z 628-1038; and mass resolution, 240 k at m/z 400 as previously described (11, 12). All the solvents used for lipids extraction and LC/MS/MS analysis are LC-MS grade from FisherScientific.

For phosphoinositide analysis 340 µl of 1 mM HCl was added at 4 °C to the cell pellet, and 10 ng of PIP$_3$ internal standard added. 750 µl of extraction mixture (484 ml of methanol, 242 ml of chloroform and 23.55 ml of 1 M HCl) was added to each sample before centrifugation (1,500 g for 5 min at 4 °C). Before further centrifugation, 725 µl of chloroform was added. The lower phase was collected and mixed with 708 µl of the upper phase of pre-derivitization wash mixture (240 ml of chloroform, 120 ml of methanol and 90 ml of 0.01 M HCl), and samples were again centrifuged. The resultant lower phase was collected. 50 µl of 2 M trimethylsilyl-diazomethane (Sigma) in hexane was added in a fume hood for 10 min at room temperature. The reaction was quenched with 6 µl of glacial acetic acid and 700 µl of the upper phase of the post-derivitization wash (240 ml of chloroform, 120 ml of methanol and 90 ml of water) added before mixing, centrifugation and collection of the lower phase. Samples were dried at room temperature and dissolved in 80 µl of methanol and 20 µl of water. Analysis was undertaken using mass spectroscopy on a QTRAP 6500

mass spectrometer (AB Sciex) connected to a Prominence high-performance liquid chromatography (HPLC) system using a 1.0 × 50 mm column (Waters) as previously described (13).

Pathway analysis. Calculation of Z score

Z-score

To calculate the Z-score the probability of x was considered in an experiment that consisted of a large number of independent trials approximated by a normal probability density

function: $\frac{1}{\sqrt{2\pi}\sigma} e^{-\left(\frac{(x-\mu)^2}{2\sigma^2}\right)}$.

A normal distributed variable x was standardised by subtracting the mean and dividing by the standard deviation of the experiment: $Z = \frac{x-\mu}{\sigma}$. This z-value or z-score described how many standard deviations (σ) of the experimental result (x) diverged from the mean of population (μ). The larger the z-score is, the less likely the experimental result is due to chance. The probability can be computed from the cumulative standard normal distribution function: $\Phi(Z) = P(Z \leq z) = \int_{-\infty}^{z} \frac{1}{\sqrt{2\pi}} e^{\frac{-u^2}{2}} du$. That gives the probability P that an experimental result with a z-score less than or equal to that observed is due to chance. Subtracting P from one: $Q = 1 - P = 1 - \Phi(Z)$ gives Q, the probability that the observed z-score is due to chance. This is by definition, a p-value. Consequently, z-score can be calculated from p-value by taking the inversed function: $Z = \Phi^{-1}(1 - Q)$.

Calculation of Z scores for the determination of active pathways was performed as follows.

Let $A = \{A_1, A_2, \dots, A_k\}$ for the pathway of interest, where A_i ($i = 1, 2, \dots, k$) are metabolites. The scoring scheme can be described in two steps. Firstly, compute a weight vector $\omega = [\omega_1, \omega_2, \dots, \omega_{k-1}]$, where $\omega_i = \frac{A_{i+1}}{A_i}$, $i = 1, 2, \dots, k - 1$. As a result, the weight for the reaction in A

9

will therefore indicate the shift toward more product or reactant in infected cells than uninfected cells. For each weighted edge of the pathway, we perform a student's t-test between the infected and baseline samples, from which a p-value is obtained (the alternative hypothesis is that the mean in infected samples is greater than that in normal samples). Assuming that the t-distribution can be approximated by a normal distribution; therefore, the p-value can be converted to Z-score by taking $Z = CDF^{-1}(1 - p)$, where CDF is the cumulative distribution function. By doing this each edge i is assigned a Z-score Z_i ($i = 1, 2, …, k - 1$). The score for pathway A is computed as follows: $Z_A = \frac{1}{\sqrt{k-1}}\sum_{i=1}^{k-1} Z_i$ As a result, $Mean(Z_A) = \frac{1}{\sqrt{k-1}}\sum_{i=1}^{k-1} Mean(Z_i) = 0, Var(Z_A) = \frac{1}{k-1}\sum_{i=1}^{k-1} Var(Z_i) = 1$

This means Z_A also follows a normal distribution. In order to check if pathway A is active (significant) in infected over healthy cells, we chose the significance level (p-value) to be 0.05, as a result, the corresponding Z-score is computed to be 1.645. Thus, if $Z_A > 1.645$ then A is classified as active.

Network Analysis was performed as follows: A complex metabolic network extracted from three databases including iRefIndex (14), HMDB (15) and Recon2 (16) was constructed. Prizes were assigned to metabolites (nodes) computed from statistical significance levels. We also assigned negative prizes (penalties) to highly connected nodes to avoid less reliable high degree connected nodes. Costs were assigned to interactions (edges) derived from the interaction probabilities. The optimization algorithm was run with different parameter sets and obtain optimal subnetworks which maximize the subnetwork robustness and the optimal subnetworks were merged into a unique optimal subnetwork.

In order to obtain independent pathways, an extra node was added to the network. This node was then connected to all terminals via edges with the same weight ω. We used the message passing approach (17) to find an optimal forest solution F with V_F nodes and E_F edges, by minimizing the sum of the total cost of all edges in the tree and the total penalties of all nodes which are not contained in the tree. The objective function for optimisation is: $f(F) = \beta \sum_{v \notin V_F} b(v) + \sum_{c \in E_F} c(e) + \omega k$

where $b(v)$ is the prize assigned to each node $v \in V_F$, $c(e)$ is the cost of each edge $e \in E_F$, k represents the number of trees in the forest F. We computed the prize for each node as –log(P value) of the significance levels of their alteration in the infected cells by two-tailed student's t-test. The cost $c(e)$ are one minus the edge weight. Here the edge weights were computed using the MIScore algorithm (18). This algorithm considers the number of publications, type of interaction and experimental methods to compute confidence scores for molecular interactions. The parameters β and ω were used to control the size of the resultant forest and the number of tree in the forest solution, respectively. In order to avoid including highly connected nodes (hub nodes) which may provide less insight information of altered pathways, we updated the prizes for all nodes in the network as follows: $b'(v) = \beta . b(v) - \mu . degree(v)$. Here μ is the parameter that controls the degree-based negative prizes. We fixed the value of ω at 50 while varying the values of β and ω to adjust the effect of terminal nodes and hub nodes in the final forest. Increasing β promoted more terminal to be included in the optimal network while increasing μ weakened the hub nodes in the optimal solution. We considered different values of β and ω in the ranges of 1 to 20 and 0.05 to 0.4, respectively, based on the input terminal sets.

For a given set of parameters (β_i, μ_i, ω) we also performed perturbation analysis to determine the robustness of the optimal forest (G_i) by generating a noisy optimal forest (T_i) obtained after adding random noise to edge weights. We then calculated a robustness score for forest (G_i) by determining a fraction of overlapping nodes between (G_i) and (T_i) as follows: $R_{G_i} = \frac{\sum_{j=1}^{N_{G_i}} f_{n_j}}{N_{G_i}}$

$f_{n_j} = \begin{cases} 1, & if \ n_j \in G_i \cup T_i \\ 0, & otherwise \end{cases}$ where for some optimal network G_i with N_{G_i} nodes, R_{G_i} shows the robustness score of forest i. After this step, all optimal forests were sorted in descending order of their robustness scores. We then used some top (or all) optimal resultant forests and merged them into a final optimal network. This optimal network therefore showed the complex interconnection of metabolic pathways. In the next step, we calculated a robustness score for each node in the final

11

optimal network: $R_{n_i} = \frac{\sum_{j=1}^{M} f_{n_i,j}}{\sum_{i=1}^{N} \sum_{j=1}^{M} f_{n_i,j}}$, $f_{n_i,j} = \begin{cases} 1, & if \ n_i \in F_j(n) \\ 0, & otherwise \end{cases}$; where for a family of M optimal

forests with N nodes, R_{n_i} represents the robustness score of node n_i $(i = 1,2,...,N)$, and F_j

represents nodes in forest j. As a result, the robustness score of a particular node is therefore

proportional to the number of times that node was selected to include in the optimal forests. After

this step, all enzymes will be sorted in descending order of their robustness scores. We then chose

some of the top enzymes for consideration. In order to compute robustness scores for edges of the

network, we considered both frequency of edge chosen for optimal networks and the probability of

interaction given by that edge. The scores for edges were therefore calculated as follows:

$R_{e_i} = \frac{p_{e_i} \cdot \sum_{j=1}^{M} f_{e_i,j}}{\sum_{i=1}^{T} \sum_{j=1}^{M} f_{e_i,j}}, f_{e_i,j} = \begin{cases} 1, & if \ n_i \in F_j(n) \\ 0, & otherwise \end{cases}$. Where for a family of M optimal forests with T edges,

R_{e_i} represents the robustness score of edge e_i $(i = 1,2,...,T)$, p_{e_i} is the probability of interaction

given by e_i, and F_j represents nodes in forest j. The edge's robustness scores are therefore show how

important that edge is in our network. As a result, this measurement was used to determine whether

a particular interaction should be highly considered over others.

RESULTS

To quantify changes in the lipidome of a relevant host cell during infection with the RV-A1b strain of

rhinovirus we established conditions where cultures of primary human bronchial epithelial cells

(HBECs) were synchronously infected with RV-1Ab. Using a high multiplicity of infection (MOI) of 20

and monitoring viral replication by expression of the viral 2C protein by confocal microscopy (Fig 1)

we showed that a time course up to 6 h post infection (hpi) produced a consistent, high percentage

(>80%) infection of HBECs without a substantial cytopathic effect.

Lipidomic analysis.

Lipid extracts were prepared from uninfected cells and HBECs infected with RV-A1b at 2, 3, 4, 5 and 6 hpi. All cultures were performed in triplicate and each experiment performed three times. Thus, data collected at each time point represents the mean of 9 samples from 3 independent experiments. The lipidomics analysis identified changes not only in the amount of a lipid class as a whole but also changes in acyl carbon chain length and saturation of individual lipid species. The analysis demonstrated changes in phospholipids, lysophospholipids, fatty acids (FA) and inositol phospholipids, in particular a significant decrease in phosphatidylcholine (PC) species and a substantial decrease in unsaturated acyl chains (acyl chains with 5,6,7 or 8 double bonds) at 6hpi (Fig. 2A). We also observed changes in phosphatidic acid (PA), diacylglycerol (DG), triglycerides (TG) and FA, fatty-acyl-CoA (FaCoA) and fatty-acyl-carnitine (FaCN). There were changes in FA species at later stages of the infection, particularly those of long fatty acyl chains (>C16) with decreases in the level of unsaturation (Fig. 2B). This implies alterations in PA, DG, TG and FA metabolism. Phosphatidylinositol (PI) is a functionally important membrane phospholipid which can be phosphorylated to phosphatidylinositol 4-phosphate (PI4P) by PI4K and subsequently to phosphatidylinositol 4,5-bisphosphate (PIP2) by phosphatidylinositol 4-phosphate 5-kinase (PIP5K). Many studies have reported the critical role of PI4K as one of the host lipid-regulatory proteins required for the viral life cycle. We observed that PI species of shorter chain (C32, C34) are more abundant in virally infected cells at the early stage of infection (2hpi) than the uninfected controls, whereas those of longer chains (>C34) with high degree of unsaturation (>2) are less abundant than in the uninfected controls. In addition at early time points we observed an increase in PI4P levels. These results are consistent with changes in PI4K activities in infected cells. The full lipidomics dataset is available as Supplementary Information Table 1.

Pathway analysis

13

Simply examining amounts of lipid species has limited benefit in understanding changes in the cell, thus we adopted a previously described method (19, 20) to search for active pathways in infected cells. This calculates statistical z-scores for all possible lipid pathways to judge whether a particular pathway is active or not. Observation of changes in the acyl chain length and number of double bonds of FAs suggested changes in FA elongation and desaturation during the viral replication cycle. Thus, we searched for active pathways of FA synthesis for which elongation and desaturation processes will be highlighted. Fig 3A shows FA synthesis pathways in which potential active pathways have been highlighted in red boxes, clearly highlighting the activation of both elongation and desaturation processes. We found no sign of active elongation and desaturation at 2hpi, whereas both processes were clearly activated at 3hpi; at later time points only the elongation process was activated. A complete set of results for active pathways of FA synthesis are summarised in Table 1 and pathway maps for the other time points are in Supplementary Figure S1. The early activated desaturation pathways (comparing 3hpi to 2hpi) correlated with a reduction in the degree of saturation of fatty acids observed (Fig 2). Additionally, the activated elongation pathways confirmed the steady increase of acyl carbon chain length seen at later stages of infection (see Fig 2 at 4,5,6 hpi).

Pathway analysis was also utilised to examine changes in lipid classes by searching for all possible active lipid pathways. Active pathways were computed for each time point as shown in Fig3. Pathway maps for all time points are in Fig S2. Table 2 shows all potentially activated and inactivated pathways in infected cells over the time course. The observed alterations in lipid pathways suggest host enzymes activities that have changed during the viral replication cycle at different time points such as PI4K being activated early (2hpi). We also observed shutting off of sphingosine-1-phosphate (S1P) synthesis and the synthesis of PC from both phosphatidylethanolamine (PE) and lysophosphatidylcholine (LPC) suggesting virus-induced alteration in membrane structure. Additionally DG, that can recruit PKD to membranes, was elevated by 2hpi with a close to significant elevation at all other time points. We repeated the lipid composition analysis comparing each time point to the control rather than

14

comparing each time point to the previous time point. This showed a consistent increase in lysophosphatidylcholine acyltransferase (LPCAT) activity at all time points whereas the S1P pathways were activated after 3hpi. Interestingly, PI4K activity was not consistently activated post infection, the increase at 2hpi was followed by a reduction in activity though the enzyme was active again at 6hpi (Table 2). These analyses also pointed to the potential activation of ceramide synthase (LASS1) and phosphatidylcholine-specific phospholipase C (PC-PLC) activities.

Network optimization

We adopted a further method, independent of pathway analysis, termed the Prize-collecting Steiner tree problem (21, 22). This aims to find an optimal forest of trees that highlights enzymes associated with potential changed pathways. In contrast to the lipid pathway analysis where only lipid classes were analysed, the Prize-collecting Steiner tree problem takes all lipid species into a complex metabolic network, which includes nodes detected in experiments (terminals) and nodes that were not detected (Steiner nodes). Those nodes (metabolites or proteins) are connected via edges representing interactions between proteins as well as substrate-enzymes and product-enzyme associations. The input to the network are metabolomics scores that differ between the infected and uninfected cells. The algorithm searches an underlying database and outputs an optimal subnetwork which shows altered viral infection-associated pathways.

The output is listed in Supplementary Table S2. As an example, Fig 4 shows part of an optimal subnetwork for the 2 hpi time point compared to the uninfected baseline time point for which associated enzymes have been highlighted. This analysis showed potential changes in the activities of the acyl transferases lysophosphatidylglycerol acyltransferase (LPGAT), lysocardiolipin acyltransferase 1 (LCLAT1), 1-acyl-sn-glycerol-3-phosphate acyltransferase (AGPAT1-6), and in ectonucleotide pyrophosphatase/phosphodiesterase 2 (ENPP2) and phospholipase A2 Group VII (PLA2G7) which generate the lysophospholipid substrates for the acyltransferases. There were also potential changes in sphingosine kinase 1 and 2 (SPHK1 and 2), sphingosine-1-phosphate phosphatase 1 (SGPP1),

15

ceramide kinase (CERK), ceramide synthase (LASS1) and sphingomyelin phosphodiesterases (SMDP1-2) enzymes regulating the concentrations of ceramide, sphingosine and S1P. Notably the enzymes highlighted from this analysis are consistent with the predictions generated by the pathway analysis. Supplemental Table S3 lists the identified enzymes.

Biological validation.

The bioinformatics analysis identified host lipid modifying enzymes whose activity changed during a single RV replication cycle. To test if these were important for viral replication we selected 18 inhibitors of enzymes and pathways identified as being of interest through our lipidomics and bioinformatics analysis. In a primary screen these compounds were tested at a final concentration of 10µM in an RV-A1b replication assay in HBECs by end point titre determination (see Fig S3). 8 compounds were identified as potential inhibitors of viral replication, these appeared to focus on the ceramide, S1P, PA and FAS pathways. These were further analysed by quantification of inhibition of viral replication by end point titre determination over a full concentration range (Fig 5) and in parallel assessed for cytotoxicity. This identified Ceranib 1, D609 and C75 as producing the most profound inhibition of viral replication at non-cytotoxic concentrations. To determine where in the viral life cycle the compounds were acting, they were tested at a single maximal non-cytotoxic concentration in infection assays measuring viral genome replication by qRT-PCR and viral protein synthesis by Western blotting with an anti-2C antibody and further confirmation by end point titre determination (Fig 6). These data show that each selected compound significantly inhibited viral genome replication and protein synthesis indicating action early in the replication cycle. To determine if the compounds were affecting viral entry by clathrin-mediated endocytosis (CME) their effects upon LDL uptake by the cells were analysed as a control, however none of the compounds had an effect (Fig 6D).

DISCUSSION

Many viruses remodel host cell intracellular membranes as part of their replicative cycle. The aim of our study was to identify RV-induced remodelling of cellular lipids in airway epithelial cells. RV is a member of the picornavirus family which includes important pathogens in animals and man including polioviruses, foot and mouth disease virus, coxsackievirus and hepatitis A virus. RV infections cause the common cold which in healthy patients is relatively trivial but in patients with asthma or COPD this can provoke serious acute worsening of their disease. We aimed to describe changes in host lipid metabolism during RV replication and use this information to identify targets in the host genome which may offer novel therapeutic targets for both RV and other RNA viruses that remodel intracellular membranes. Whilst the literature contains reports of virus-induced changes in lipids, for example H1N1 influenza infection of mouse lung tissue (23) and rotavirus-infected MA104 cells (9), no study has utilised pathway analysis and other bioinformatics approaches to identify potential molecular targets.

Picornaviruses induce massive remodeling of intracellular membranes into clusters of double membrane bound vesicles with a diameter of 200-400nm resembling autophagosomes (24-27). Despite differences between members of the picornavirus family, there are common features with polioviruses being the best studied. Polioviruses disrupt traffic through the secretory pathway and the 2B and 3A non-structural viral proteins, when expressed individually, disrupt the morphology of ER and Golgi and influence the transit of protein cargo (8, 28-30). The profound remodelling of host membranes has suggested that lipid modifying enzymes might be promising anti-viral targets (31). Several examples support this concept. This may in part be through altering the function of Arf1 in. Brefeldin A, a drug that inhibits the GTP exchange factor required for Arf1 activation (GBF1) and alters COP-I recruitment to membranes (32, 33), impedes the replication of several picornaviruses (34, 35), including RV (data not shown). Phospholipase D (PLD), an enzyme whose activity is also regulated by Arf1 and implicated in the regulation of membrane trafficking (36), was one of the enzymes identified by our pathway analysis as activated by RV (Table 2) thereby adding additional mechanistic insight

17

into the role of Arf1 in viral replication. Positive strand RNA viruses such as enteroviruses and flaviviruses recruit host phosphatidylinositol-4-kinase IIIβ (PI4KB) and the viral RNA polymerase (3Dpol) binds PI4P and assembles on PI4P enriched membranes (2). The picornaviral 3A protein can associate with the Golgi proteins ACBD3 (GCP60) and PI4KIIIβ (37-40) and PI4KIIIβ has been shown to be the target of certain anti-polio drugs (41-43). A number of additional host proteins interacting with the picornavirus 3A protein have been identified including VAMP-associated protein-A (VAP-A) (37) an ER protein essential for the stimulation of sphingomyelin (SM) synthesis by 25-hydroxycholesterol (44, 45) and depletion of VAPs by RNAi reduces the levels of PI4P, DG, and SM in the Golgi membranes (46). VAP-A binds OSBP, a family of lipid transfer proteins that control cholesterol/PI4P exchange at ER-Golgi membrane contact sites and also bind Arf1. OSBP is also targeted by certain anti-picornaviral drugs (4, 6, 47) providing further evidence for the requirement for lipid homeostasis at the ER/Golgi interface for viral replication. Additionally, the anti-viral effector protein interferon-inducible transmembrane protein 3 (IFITM3) interacts with VAP-A and prevents its association with OSBP thereby disrupting intracellular cholesterol homeostasis and inhibiting viral entry (48). Thus multiple lines of evidence point to PI4P being a pivotal ER/Golgi phospholipid in viral replication. Our data confirms viral replication influences PI4Ks activity (Figure 3, Table 2), but notably our analysis highlights distinct phases of activation at both 2 and 6 hpi, with no increase during the intervening period, pointing to a more complex regulation of phosphoinositide signaling than previously

Changes in other lipids are implicated in viral replication, for example poliovirus stimulates PC synthesis through activation of CTP:phosphocholine cytidylyltransferase (49) and inhibitors of phospholipid biosynthesis such as cerulenin block poliovirus replication (50). Recently it has been shown that picornavirus infection induces FA import which is linked to PC synthesis and the formation of replication complexes. This is linked to long chain fatty acyl-CoA synthetase activity, a host factor required for poliovirus replication (51). Early events such as viral entry to cells induce activation of sphingomyelinase and the creation of ceramide rich patches on the plasma membrane (52) and

picornaviruses also cause redistribution of cellular cholesterol to replication complexes which is critical for completion of the viral life cycle (53).

In our unbiased lipidomics approach we have performed a time course of a synchronous infection of RV in primary human bronchial epithelial cells. The results show widespread perturbation of lipid metabolic pathways with clear effects of increased FA elongation and desaturation with time and increases in long chain fatty acids (C22, C24) particularly at 5,6 hpi (Fig. 2). Pathway analysis also suggests that between 2 and 3 hpi there are increases in lysocardiolipin acyltransferase (LPIAT), phosphoinositides phosphatase (PIP), DG kinase, LPCAT activities and decrease in phosphoinositide phospholipase (PI-PLA), phosphatidylcholine phospholipase (PC-PLA), SPHK1 and 2 and phosphatidylglycerophosphate synthase (PGPS) activities. Between 3 and 4 hpi there are probable increases in PI3K and LASS1 activities. Between 4 and 5 hpi there are decreases in phosphatidylserine synthase-1 (PSS1), PI3K and between 5 and 6 hpi increases in LPCAT and PLD activities. The clear changes detected at 2 hpi, in particular, strongly suggest that the virus is affecting enzyme activities directly, whilst at later times it is probable that there are additional effects including upon enzyme synthesis, presumably mediated through regulation of SREBP activity. The number and complexity of the observed changes does not clearly lead to a single mechanistic understanding of how or why viral replication is inducing such profound changes in the host lipidome. However it does generate a number of testable hypotheses.

We have previously shown that PKD is activated late in the RV replication cycle and that PKD inhibitors reduce RV replication (7). Since PKD is a DG activated kinase, our time course and pathway analysis showing changes in flux through DG pathways are consistent with our previous observations: our data shows an activation of DG kinase activity in which DG – a recruiter of PKD was elevated by 2hpi.

To test if the highlighted lipid signalling and metabolic pathways were important for viral replication and not merely a consequence of replication, we chose chemical inhibitor tools for target validation rather than siRNA as we find administration of RNA or DNA into cells activates the innate anti-viral

host response which profoundly interferes with RV replication. The validation studies identified Ceranib 1, D609 and C75 as significant RV replication inhibitors at concentrations not cytotoxic to the host cells. D609, whilst reported to be non-specific, inhibits PC-PLC and SMS (54) which both produce DG from PC, consistent with a role for DG and thus potentially PKD in RV replication. Our pathway analysis shows a potential increase in PC-PLC activity as well as activation of sphingomyelin synthase activity (at 6hpi) producing DG and sphingomyelin. On the other hand, our network optimisation shows potential changes in sphingomyelin phosphodiesterase (SMPD) which could suggest changes in sphingomyelin synthase activity as well.

The lipidomics revealed substantial FA modifications, both acyl chain length and saturation and in keeping with this C75, a FAS inhibitor was an effective inhibitor of RV replication (Figure 5). Nchoutmboube et al showed that PV induces the uptake of FA that have 16 or 18C and that this matches the membrane properties of the replication complexes (51). Furthermore, FAS has been described as an anti-viral target for coxackievirus B3 (CVB3) (55) indeed amentoflavone, a FAS inhibitor, reduced CVB3 replication (56). Therefore, our observation for the importance of FAS in RV replication is consistent with studies on other viruses including picornaviruses. Ceranib 1 inhibits ceramidase which cleaves FA from ceramide, producing sphingosine which is phosphorylated by sphingosine kinase leading to S1P. Our pathway analysis shows potential activation of ceramide synthase activity at 4hpi whereas the network optimisation method suggests possible changes in ceramide kinase (CERK) and ceramide synthase (LASS1) across all time points. In addition, when comparing later time points with the baseline time point, there were consistent increases in S1P phosphatase and potentially in ceramide synthase activities. Our findings are consistent with observations from other viruses, for example inhibitors of SM biosynthesis affect HCV replication (57), and SM localises to WNV replication complexes and viral replication is moderately affected by SM biosynthesis inhibition (58). Ceramide has been shown to redistribute to WNV replication complexes and the inhibition of ceramide synthesis impairs replication (59). Thus lipidomics with pathway analysis identified novel therapeutic targets to antagonise RV infection. The inhibitors we have

identified blocked replication of the viral genome (Fig 6A) and consequently production of viral proteins (Fig 6B), thus they are acting early in the viral replication cycle. Importantly, the active inhibitors were not preventing viral entry, as assessed by monitoring CME, and thus the site of action is predicted to be between viral entry and genome replication, so confirming the importance of lipid metabolism in this process. It will be important, nevertheless, to determine the roles these enzymes and associated lipid changes play in viral infection and replication.

In summary, we have performed an unbiased lipidomic study of primary HBECs infected with RV and analysed changes in lipid composition during a single round of viral replication. We have identified significant alterations in multiple pathways which change with time in a complex fashion, these have only been revealed by performing a time course in synchronously infected cells. Based on our network and pathway analysis, we identified a number of potentially important enzymes involved in the observed lipid metabolic changes and using chemical inhibitors we have shown that PC-PLC, SMS and FAS are of interest in this respect and worthy of further study as potential therapeutic targets.

References

1. Wessels, E., D. Duijsings, K. H. Lanke, S. H. van Dooren, C. L. Jackson, W. J. Melchers, and F. J. van Kuppeveld. 2006. Effects of picornavirus 3A Proteins on Protein Transport and GBF1-dependent COP-I recruitment. *J Virol* **80**: 11852-11860.

2.   Hsu, N. Y., O. Ilnytska, G. Belov, M. Santiana, Y. H. Chen, P. M. Takvorian, C. Pau, H. van der Schaar, N. Kaushik-Basu, T. Balla, C. E. Cameron, E. Ehrenfeld, F. J. van Kuppeveld, and N. Altan-Bonnet. 2010. Viral reorganization of the secretory pathway generates distinct organelles for RNA replication. *Cell* **141**: 799-811.

3.   Spickler, C., J. Lippens, M. K. Laberge, S. Desmeules, E. Bellavance, M. Garneau, T. Guo, O. Hucke, P. Leyssen, J. Neyts, F. H. Vaillancourt, A. Decor, J. O'Meara, M. Franti, and A. Gauthier. 2013. Phosphatidylinositol 4-kinase III beta is essential for replication of human rhinovirus and its inhibition causes a lethal phenotype in vivo. *Antimicrob Agents Chemother* **57**: 3358-3368.

4.   Albulescu, L., J. R. Strating, H. J. Thibaut, L. van der Linden, M. D. Shair, J. Neyts, and F. J. van Kuppeveld. 2015. Broad-range inhibition of enterovirus replication by OSW-1, a natural compound targeting OSBP. *Antiviral Res* **117**: 110-114.

5.   Arita, M., H. Kojima, T. Nagano, T. Okabe, T. Wakita, and H. Shimizu. 2013. Oxysterol-binding protein family I is the target of minor enviroxime-like compounds. *J Virol* **87**: 4252-4260.

6.   Strating, J. R., L. van der Linden, L. Albulescu, J. Bigay, M. Arita, L. Delang, P. Leyssen, H. M. van der Schaar, K. H. Lanke, H. J. Thibaut, R. Ulferts, G. Drin, N. Schlinck, R. W. Wubbolts, N. Sever, S. A. Head, J. O. Liu, P. A. Beachy, M. A. De Matteis, M. D. Shair, V. M. Olkkonen, J. Neyts, and F. J. van Kuppeveld. 2015. Itraconazole inhibits enterovirus replication by targeting the oxysterol-binding protein. *Cell Rep* **10**: 600-615.

7.   Guedan, A., D. Swieboda, M. Charles, M. Toussaint, S. L. Johnston, A. Asfor, A. Panjwani, T. J. Tuthill, H. Danahay, T. Raynham, A. Mousnier, and R. Solari. 2017. Investigation of the Role of Protein Kinase D in Human Rhinovirus Replication. *J Virol* **91**: e00217-00217.

8.   Mousnier, A., D. Swieboda, A. Pinto, A. Guedan, A. V. Rogers, R. Walton, S. L. Johnston, and R. Solari. 2014. Human rhinovirus 16 causes Golgi apparatus fragmentation without blocking protein secretion. *J Virol* **88**: 11671-11685.

9.   Gaunt, E., Q. Zhang, W. Cheung, M. J. O. Wakelam, A. Lever, and U. Desselberger. 2013. Lipidome analysis of rotavirus infected cells by mass spectrometry. *J. Gen. Virol.* **94**: 1576-1586.

10.   Liefhebber, J. M., C. V. Hague, Q. Zhang, M. J. Wakelam, and J. McLauchlan. 2014. Modulation of triglyceride and cholesterol ester synthesis impairs assembly of infectious hepatitis C virus. *J Biol Chem* **289**: 21276-21288.

11.   Sanchez-Alvarez, M., Q. Zhang, F. Finger, M. J. Wakelam, and C. Bakal. 2015. Cell cycle progression is an essential regulatory component of phospholipid metabolism and membrane homeostasis. *Open biology* **5**: 150093.

12.   Peck, B., Z. T. Schug, Q. Zhang, B. Dankworth, D. T. Jones, E. Smethurst, R. Patel, S. Mason, M. Jiang, R. Saunders, M. Howell, R. Mitter, B. Spencer-Dene, G. Stamp, L. McGarry, D. James, E. Shanks, E. O. Aboagye, S. E. Critchlow, H. Y. Leung, A. L. Harris, M. J. Wakelam, E. Gottlieb, and A. Schulze. 2016. Inhibition of fatty acid desaturation is detrimental to cancer cell survival in metabolically compromised environments. *Cancer & metabolism* **4**: 6.

13.   Clark, J., K. E. Anderson, V. Juvin, T. S. Smith, F. Karpe, M. J. O. Wakelam, L. R. Stephens, and P. T. Hawkins. 2011. Quantification of PtdInsP$_3$ molecular species in cells and tissues by mass spectrometry. *Nature Methods* **8**: 267-272.

14.   Razick, S., G. Magklaras, and I. M. Donaldson. 2008. iRefIndex: a consolidated protein interaction database with provenance. *BMC Bioinformatics* **9**: 405.

15.   Wishart, D. S., T. Jewison, A. C. Guo, M. Wilson, C. Knox, Y. Liu, Y. Djoumbou, R. Mandal, F. Aziat, E. Dong, S. Bouatra, I. Sinelnikov, D. Arndt, J. Xia, P. Liu, F. Yallou, T. Bjorndahl, R. Perez-Pineiro, R. Eisner, F. Allen, V. Neveu, R. Greiner, and A. Scalbert. 2013. HMDB 3.0--The Human Metabolome Database in 2013. *Nucleic Acids Res* **41**: D801-807.

16.   Thiele, I., N. Swainston, R. M. Fleming, A. Hoppe, S. Sahoo, M. K. Aurich, H. Haraldsdottir, M. L. Mo, O. Rolfsson, M. D. Stobbe, S. G. Thorleifsson, R. Agren, C. Bolling, S. Bordel, A. K. Chavali, P. Dobson, W. B. Dunn, L. Endler, D. Hala, M. Hucka, D. Hull, D. Jameson, N. Jamshidi, J. J. Jonsson, N. Juty, S. Keating, I. Nookaew, N. Le Novere, N. Malys, A. Mazein, J. A. Papin, N. D. Price, E. Selkov, Sr., M. I. Sigurdsson, E. Simeonidis, N. Sonnenschein, K. Smallbone, A. Sorokin, J. H. van Beek, D.

Weichart, I. Goryanin, J. Nielsen, H. V. Westerhoff, D. B. Kell, P. Mendes, and B. O. Palsson. 2013. A community-driven global reconstruction of human metabolism. *Nat Biotechnol* **31**: 419-425.

17.   Bailly-Bechet, M., A. Braunstein, A. Pagnani, M. Weigt, and R. Zecchina. 2010. Inference of sparse combinatorial-control networks from gene-expression data: a message passing approach. *BMC Bioinformatics* **11**: 355.

18.   Aranda, B., H. Blankenburg, S. Kerrien, F. S. Brinkman, A. Ceol, E. Chautard, J. M. Dana, J. De Las Rivas, M. Dumousseau, E. Galeota, A. Gaulton, J. Goll, R. E. Hancock, R. Isserlin, R. C. Jimenez, J. Kerssemakers, J. Khadake, D. J. Lynn, M. Michaut, G. O'Kelly, K. Ono, S. Orchard, C. Prieto, S. Razick, O. Rigina, L. Salwinski, M. Simonovic, S. Velankar, A. Winter, G. Wu, G. D. Bader, G. Cesareni, I. M. Donaldson, D. Eisenberg, G. J. Kleywegt, J. Overington, S. Ricard-Blum, M. Tyers, M. Albrecht, and H. Hermjakob. 2011. PSICQUIC and PSISCORE: accessing and scoring molecular interactions. *Nat Methods* **8**: 528-529.

19.   Ideker, T., O. Ozier, B. Schwikowski, and A. F. Siegel. 2002. Discovering regulatory and signalling circuits in molecular interaction networks. *Bioinformatics* **18 Suppl 1**: S233-240.

20.   Lee, E., H.-Y. Chuang, J.-W. Kim, T. Ideker, and D. Lee. 2008. Inferring Pathway Activity toward Precise Disease Classification. *PLOS Computational Biology* **4**: e1000217.

21.   Biazzo, I., A. Braunstein, and R. Zecchina. 2012. Performance of a cavity-method-based algorithm for the prize-collecting Steiner tree problem on graphs. *Phys Rev E Stat Nonlin Soft Matter Phys* **86**: 026706.

22.   Pirhaji, L., P. Milani, M. Leidl, T. Curran, J. Avila-Pacheco, C. B. Clish, F. M. White, A. Saghatelian, and E. Fraenkel. 2016. Revealing disease-associated pathways by network integration of untargeted metabolomics. *Nat Methods* **13**: 770-776.

23.   Woods, P. S., L. M. Doolittle, L. E. Rosas, L. M. Joseph, E. P. Calomeni, and I. C. Davis. 2016. Lethal H1N1 influenza A virus infection alters the murine alveolar type II cell surfactant lipidome. *Am J Physiol Lung Cell Mol Physiol* **311**: L1160-l1169.

24.   Bienz, K., D. Egger, T. Pfister, and M. Troxler. 1992. Structural and functional characterization of the poliovirus replication complex. *J Virol* **66**: 2740-2747.

25.   Schlegel, A., T. H. Giddings, Jr., M. S. Ladinsky, and K. Kirkegaard. 1996. Cellular origin and ultrastructure of membranes induced during poliovirus infection. *J Virol* **70**: 6576-6588.

26.   Suhy, D. A., T. H. Giddings, Jr., and K. Kirkegaard. 2000. Remodeling the endoplasmic reticulum by poliovirus infection and by individual viral proteins: an autophagy-like origin for virus-induced vesicles. *J Virol* **74**: 8953-8965.

27.   Taylor, M. P., and K. Kirkegaard. 2008. Potential subversion of autophagosomal pathway by picornaviruses. *Autophagy* **4**: 286-289.

28.   Doedens, J. R., T. H. Giddings, Jr., and K. Kirkegaard. 1997. Inhibition of endoplasmic reticulum-to-Golgi traffic by poliovirus protein 3A: genetic and ultrastructural analysis. *J Virol* **71**: 9054-9064.

29.   Doedens, J. R., and K. Kirkegaard. 1995. Inhibition of cellular protein secretion by poliovirus proteins 2B and 3A. *Embo j* **14**: 894-907.

30.   Sandoval, I. V., and L. Carrasco. 1997. Poliovirus infection and expression of the poliovirus protein 2B provoke the disassembly of the Golgi complex, the organelle target for the antipoliovirus drug Ro-090179. *J Virol* **71**: 4679-4693.

31.   Altan-Bonnet, N. 2017. Lipid Tales of Viral Replication and Transmission. *Trends Cell Biol* **27**: 201-213.

32.   Belov, G. A., C. Habbersett, D. Franco, and E. Ehrenfeld. 2007. Activation of cellular Arf GTPases by poliovirus protein 3CD correlates with virus replication. *J Virol* **81**: 9259-9267.

33.   van der Linden, L., H. M. van der Schaar, K. H. Lanke, J. Neyts, and F. J. van Kuppeveld. 2010. Differential effects of the putative GBF1 inhibitors Golgicide A and AG1478 on enterovirus replication. *J Virol* **84**: 7535-7542.

34.   Belov, G. A., M. H. Fogg, and E. Ehrenfeld. 2005. Poliovirus proteins induce membrane association of GTPase ADP-ribosylation factor. *J Virol* **79**: 7207-7216.

35. Lanke, K. H., H. M. van der Schaar, G. A. Belov, Q. Feng, D. Duijsings, C. L. Jackson, E. Ehrenfeld, and F. J. van Kuppeveld. 2009. GBF1, a guanine nucleotide exchange factor for Arf, is crucial for coxsackievirus B3 RNA replication. *J Virol* **83**: 11940-11949.

36. McDermott, M., M. J. O. Wakelam, and A. J. Morris. 2004. Phospholipase D. *Biochemistry and Cell Biology* **82**: 225-253.

37. Greninger, A. L., G. M. Knudsen, M. Betegon, A. L. Burlingame, and J. L. Derisi. 2012. The 3A protein from multiple picornaviruses utilizes the golgi adaptor protein ACBD3 to recruit PI4KIIIbeta. *J Virol* **86**: 3605-3616.

38. Lei, X., X. Xiao, Z. Zhang, Y. Ma, J. Qi, C. Wu, Y. Xiao, Z. Zhou, B. He, and J. Wang. 2017. The Golgi protein ACBD3 facilitates Enterovirus 71 replication by interacting with 3A. *Sci Rep* **7**: 44592.

39. Sasaki, J., K. Ishikawa, M. Arita, and K. Taniguchi. 2012. ACBD3-mediated recruitment of PI4KB to picornavirus RNA replication sites. *Embo j* **31**: 754-766.

40. Xiao, X., X. Lei, Z. Zhang, Y. Ma, J. Qi, C. Wu, Y. Xiao, L. Li, B. He, and J. Wang. 2017. Enterovirus 3A facilitates viral replication by promoting PI4KB-ACBD3 interaction. *J Virol* **91**: e00791-00717.

41. Arita, M., H. Kojima, T. Nagano, T. Okabe, T. Wakita, and H. Shimizu. 2011. Phosphatidylinositol 4-kinase III beta is a target of enviroxime-like compounds for antipoliovirus activity. *J Virol* **85**: 2364-2372.

42. Ford Siltz, L. A., E. G. Viktorova, B. Zhang, D. Kouiavskaia, E. Dragunsky, K. Chumakov, L. Isaacs, and G. A. Belov. 2014. New small-molecule inhibitors effectively blocking picornavirus replication. *J Virol* **88**: 11091-11107.

43. van der Schaar, H. M., P. Leyssen, H. J. Thibaut, A. de Palma, L. van der Linden, K. H. Lanke, C. Lacroix, E. Verbeken, K. Conrath, A. M. Macleod, D. R. Mitchell, N. J. Palmer, H. van de Poel, M. Andrews, J. Neyts, and F. J. van Kuppeveld. 2013. A novel, broad-spectrum inhibitor of enterovirus replication that targets host cell factor phosphatidylinositol 4-kinase IIIbeta. *Antimicrob Agents Chemother* **57**: 4971-4981.

44. Furuita, K., J. Jee, H. Fukada, M. Mishima, and C. Kojima. 2010. Electrostatic interaction between oxysterol-binding protein and VAMP-associated protein A revealed by NMR and mutagenesis studies. *J Biol Chem* **285**: 12961-12970.

45. Wyles, J. P., and N. D. Ridgway. 2004. VAMP-associated protein-A regulates partitioning of oxysterol-binding protein-related protein-9 between the endoplasmic reticulum and Golgi apparatus. *Exp Cell Res* **297**: 533-547.

46. Peretti, D., N. Dahan, E. Shimoni, K. Hirschberg, and S. Lev. 2008. Coordinated lipid transfer between the endoplasmic reticulum and the Golgi complex requires the VAP proteins and is essential for Golgi-mediated transport. *Mol Biol Cell* **19**: 3871-3884.

47. Albulescu, L., J. Bigay, B. Biswas, M. Weber-Boyvat, C. M. Dorobantu, L. Delang, H. M. van der Schaar, Y. S. Jung, J. Neyts, V. M. Olkkonen, F. J. van Kuppeveld, and J. R. Strating. 2017. Uncovering oxysterol-binding protein (OSBP) as a target of the anti-enteroviral compound TTP-8307. *Antiviral Res* **140**: 37-44.

48. Amini-Bavil-Olyaee, S., Y. J. Choi, J. H. Lee, M. Shi, I. C. Huang, M. Farzan, and J. U. Jung. 2013. The antiviral effector IFITM3 disrupts intracellular cholesterol homeostasis to block viral entry. *Cell Host Microbe* **13**: 452-464.

49. Vance, D. E., E. M. Trip, and H. B. Paddon. 1980. Poliovirus increases phosphatidylcholine biosynthesis in HeLa cells by stimulation of the rate-limiting reaction catalyzed by CTP: phosphocholine cytidylyltransferase. *J Biol Chem* **255**: 1064-1069.

50. Guinea, R., and L. Carrasco. 1990. Phospholipid biosynthesis and poliovirus genome replication, two coupled phenomena. *Embo j* **9**: 2011-2016.

51. Nchoutmboube, J. A., E. G. Viktorova, A. J. Scott, L. A. Ford, Z. Pei, P. A. Watkins, R. K. Ernst, and G. A. Belov. 2013. Increased long chain acyl-Coa synthetase activity and fatty acid import is linked to membrane synthesis for development of picornavirus replication organelles. *PLoS Pathog* **9**: e1003401.

52.   Grassme, H., A. Riehle, B. Wilker, and E. Gulbins. 2005. Rhinoviruses infect human epithelial cells via ceramide-enriched membrane platforms. *J Biol Chem* **280**: 26256-26262.

53.   Ilnytska, O., M. Santiana, N. Y. Hsu, W. L. Du, Y. H. Chen, E. G. Viktorova, G. Belov, A. Brinker, J. Storch, C. Moore, J. L. Dixon, and N. Altan-Bonnet. 2013. Enteroviruses harness the cellular endocytic machinery to remodel the host cell cholesterol landscape for effective viral replication. *Cell Host Microbe* **14**: 281-293.

54.   Adibhatla, R. M., J. F. Hatcher, and A. Gusain. 2012. Tricyclodecan-9-yl-xanthogenate (D609) mechanism of actions: a mini-review of literature. *Neurochem Res* **37**: 671-679.

55.   Rassmann, A., A. Henke, N. Jarasch, F. Lottspeich, H. P. Saluz, and T. Munder. 2007. The human fatty acid synthase: a new therapeutic target for coxsackievirus B3-induced diseases? *Antiviral Res* **76**: 150-158.

56.   Wilsky, S., K. Sobotta, N. Wiesener, J. Pilas, N. Althof, T. Munder, P. Wutzler, and A. Henke. 2012. Inhibition of fatty acid synthase by amentoflavone reduces coxsackievirus B3 replication. *Arch Virol* **157**: 259-269.

57.   Hirata, Y., K. Ikeda, M. Sudoh, Y. Tokunaga, A. Suzuki, L. Weng, M. Ohta, Y. Tobita, K. Okano, K. Ozeki, K. Kawasaki, T. Tsukuda, A. Katsume, Y. Aoki, T. Umehara, S. Sekiguchi, T. Toyoda, K. Shimotohno, T. Soga, M. Nishijima, R. Taguchi, and M. Kohara. 2012. Self-enhancement of hepatitis C virus replication by promotion of specific sphingolipid biosynthesis. *PLoS Pathog* **8**: e1002860.

58.   Martin-Acebes, M. A., E. Gabande-Rodriguez, A. M. Garcia-Cabrero, M. P. Sanchez, M. D. Ledesma, F. Sobrino, and J. C. Saiz. 2016. Host sphingomyelin increases West Nile virus infection in vivo. *J Lipid Res* **57**: 422-432.

59.   Aktepe, T. E., H. Pham, and J. M. Mackenzie. 2015. Differential utilisation of ceramide during replication of the flaviviruses West Nile and dengue virus. *Virology* **484**: 241-250.

Table 1. Active pathways of fatty acid synthesis. The data represents three independent experiments each performed in triplicate. FA composition at each time point was compared to the previous time point and pathway analysis performed. Pathways with a Z-score >1.645 are considered active.

time point (current hpi /previous hpi)	Pathway	Z-Score	Processes
2/0	18:0-FA->18:1-FA->18:2-FA->18:3-FA->20:3-FA->20:4-FA->22:4-FA	-2.82	Decreases in elongation and desaturation
	20:4-FA->22:4-FA	-2.39	
	16:0-FA->16:1-FA	-2.10	
	18:1-FA->18:2-FA	-1.85	
	20:0-FA->20:1-FA	-1.75	
	18:0-FA->18:1-FA->18:2-FA->18:3-FA->20:3-FA->20:4-FA->20:5-FA->22:5-FA	-1.66	
3/2	16:1-FA->18:1-FA->18:2-FA->18:3-FA->20:3-FA->20:4-FA->22:4-FA	2.80	Changes in elongation and increase in desaturation
	20:4-FA->22:4-FA	1.86	
	18:0-FA->20:0-FA	1.86	
	18:1-FA->18:2-FA	1.75	
	24:0-FA->26:0-FA	-1.97	

	20:0-FA->22:0-FA	-19.4	
	20:1-FA->22:1-FA	-1.65	
4/3	18:1-FA->20:1-FA->22:1-FA->24:1-FA	1.93	Increase in elongation
	16:0-FA->18:0-FA	1.71	
5/4	18:1-FA->20:1-FA	2.22	Increase in elongation
	18:0-FA->20:0-FA	2.21	
6/5	22:0-FA->24:0-FA->26:0-FA	2.70	Increase in elongation and decrease in desaturation
	22:1-FA->24:1-FA	2.35	
	18:1-FA->20:1-FA	2.22	
	24:0-FA->26:0-FA	1.95	
	16:0-FA->16:1-FA->18:1-FA->18:2-FA->18:3-FA->20:3-FA->20:4-FA->20:5-FA->22:5-FA	-3.07	
	16:1-FA->18:1-FA->18:2-FA->18:3-FA->20:3-FA	-2.60	
	18:0-FA->18:1-FA->18:2-FA->18:3-FA->20:3-FA->20:4-FA->20:5-FA->22:5-FA	-2.46	
	16:0-FA->16:1-FA->18:1-FA->18:2-FA->18:3-FA->20:3-FA->20:4-FA->22:4-FA	-2.12	

	18:2-FA->18:3-FA	-1.97	
	20:0-FA->20:1-FA->22:1-FA	-1.92	

Table 2. Active lipid metabolic pathways. Lipid composition at a time point was compared to the previous time point and pathway analysis performed. Pathway Z-score >1.645 is significantly upregulated whilst a negative Z-score <-1.645 is significantly downregulated. Data represent three independent experiments performed in triplicate.

time point (current hpi /previous hpi)	Pathway	ZScore	Predicted enzymes activities
2/0	PA->PI->LPI	2.53	Increase in LPCAT, PI4-kinase, PI-PLA, PA phosphatase, PS synthase and PTEN activities and decrease in PI3kinase, DG kinase activities. Potential increase in PC-PLC.
	PI -> PIP	2.46	
	PA->PI->PIP->PIP2	2.21	
	LPC->PC->DG	2.30	
	PA->PS->PE->PC->DG	2.21	
	PI->LPI	1.78	
	DG->PA	-1.73	
	PIP2->PIP3	-2.51	
3/2	LPI->PI	2.46	Increase in LPIAT, PIP phosphatase, DG kinase, LPCAT activities and decrease in PI-PLA, PC-PLA, sphingosine kinase,
	LPC->PC	2.24	
	DG->PA	1.96	
	PA->PG	-1.78	
	SG->S1P	-1.84	

29

			PGP synthase activities.
4/3	PI->LPI	1.77	Probable increase in PI3kinase and ceramide synthase activities.
	PIP2->PIP3	1.54	
	SG->Cer	1.54	
5/4	PIP2->PIP3	-1.55	Decrease in PS synthase 1, PI3kinase.
	PC->PS	-1.97	
6/5	LPC->PC->PA->PI->PIP->PIP2->PIP3	2.58	Increase in PI3kinase, LPCAT, PLD and Sphingomyelin synthase activities. Potential increase in PC-PLC.
	LPC->PC->DG	2.40	
	LPC->PC->PA->PI->LPI	2.23	
	LPC->PC->PA->PG	2.00	
	PC->PA	1.87	
	LPC->PC->PA->PS->PE	1.76	
	LPC->PC->PA->DG->TG	1.67	
	PC + Cer -> SM + DG	1.66	
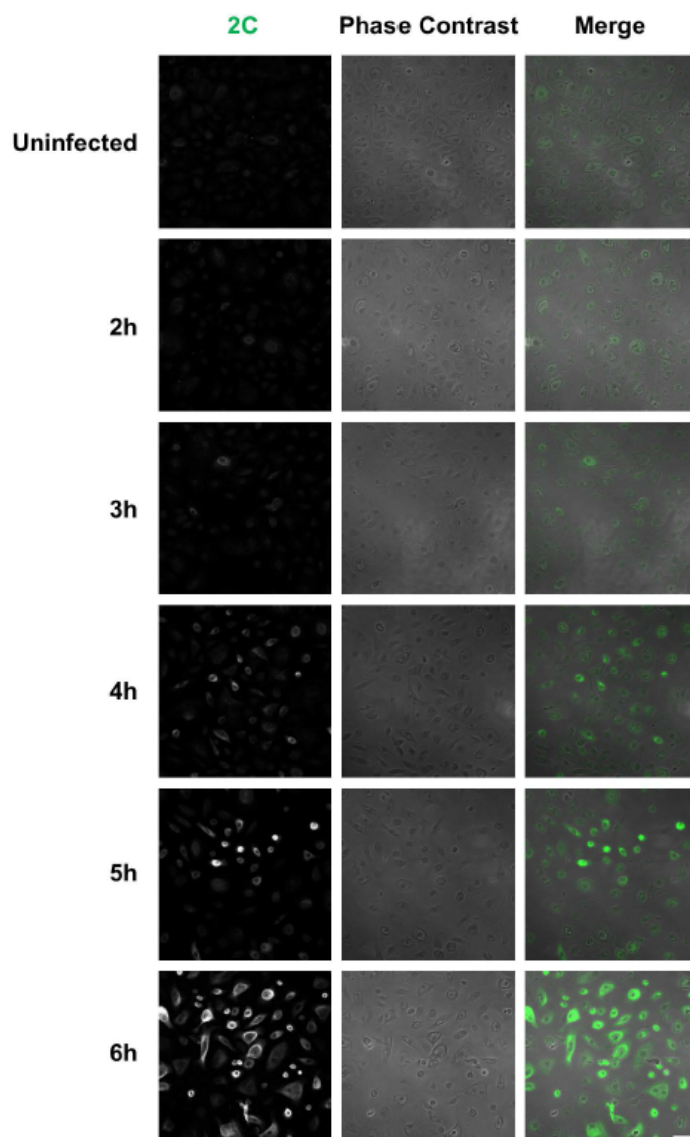
Figure 1. Infection of primary human bronchial epithelial cells with RV-A1b. Confluent primary

human bronchial epithelial cells were infected with RV-A1b at an MOI of 20 for 1h, after unbound

virus removal, replication proceeded for up to 6hpi. Cells were fixed and processed for confocal

microscopy by staining with anti-RV 2C protein. Each column shows the 2C staining, the phase
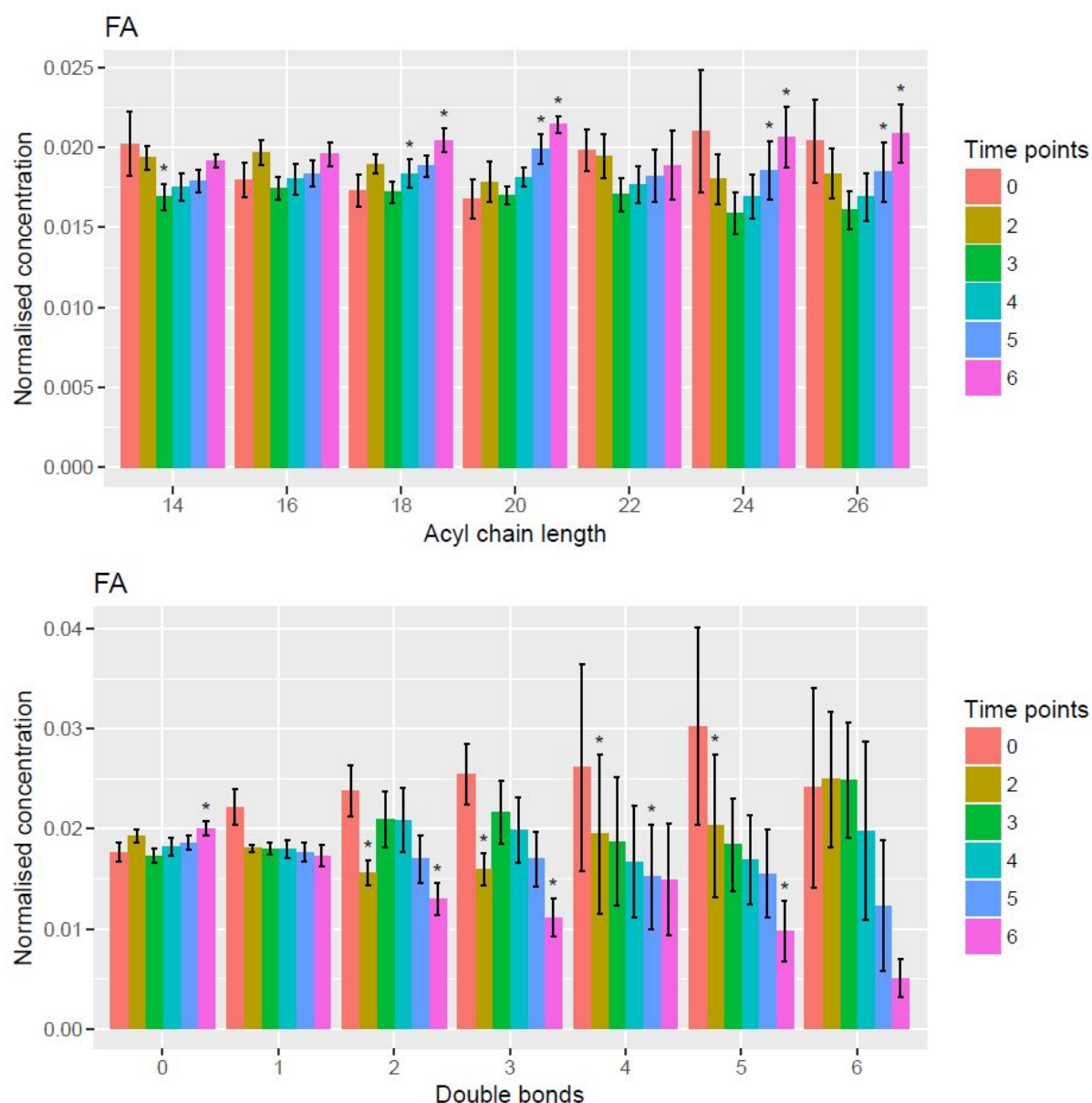
contrast and merged images. Scalebar represents 50μm.

A
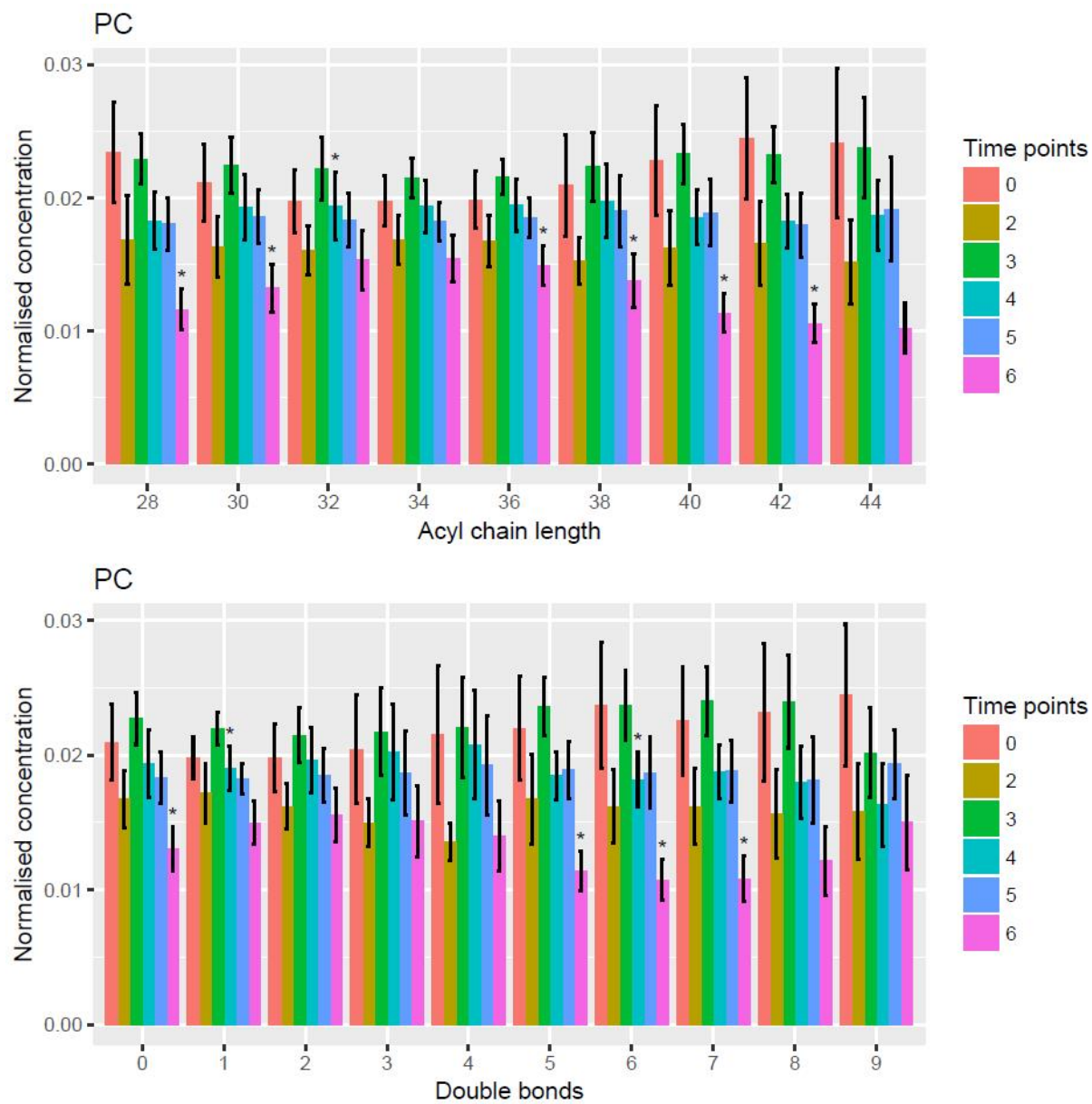
B

Figure 2. **Changes in (A) PC and (B) FA structures during the 6 hours viral replication timecourse**.

The figure shows changes in both acyl chain length and saturation of PC and FA, concentrations were

normalised in each group to cell number. Each time point represents the mean +/- SEM from three

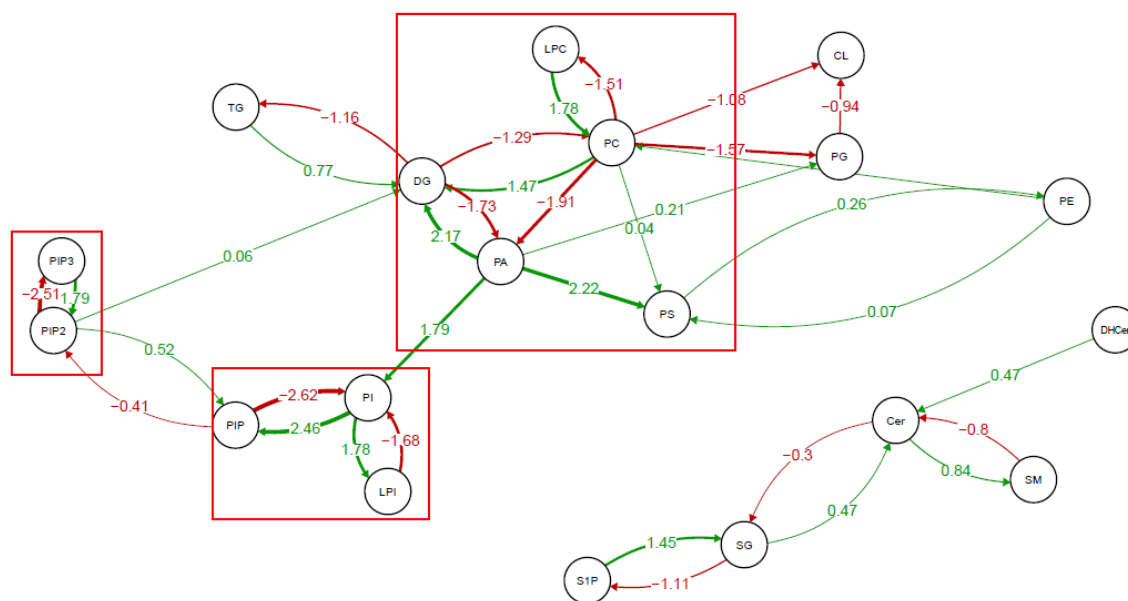independent experiments performed in triplicate (n=9) per time point (* = P<0.05 by student's t-

test).

A
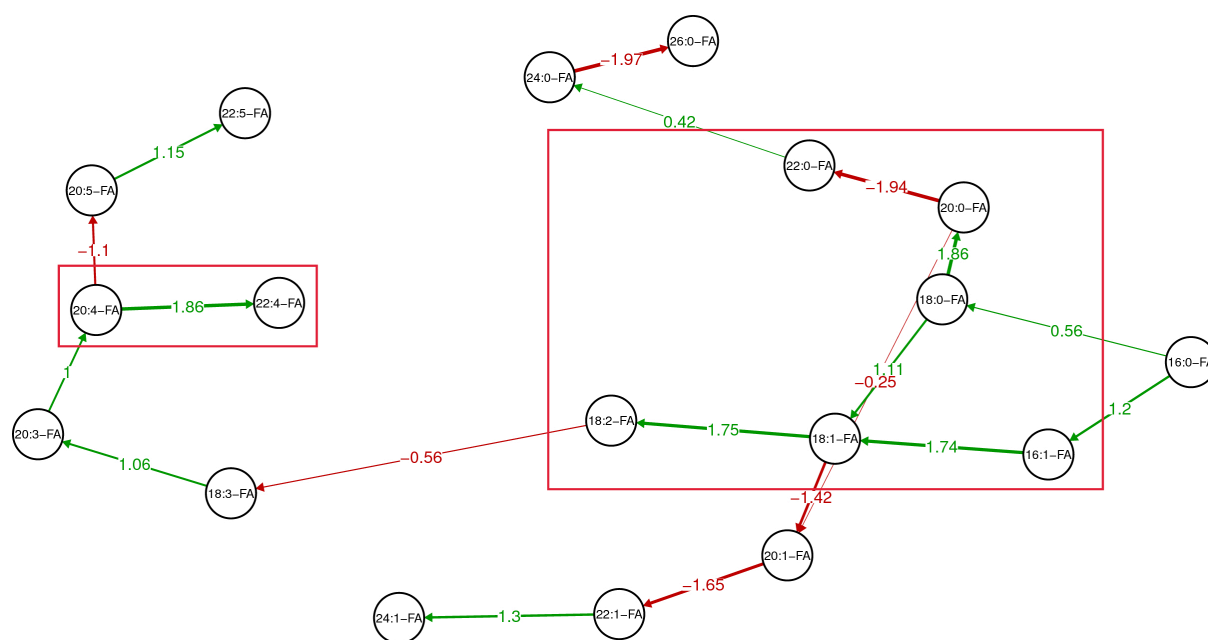
B

Figure 3. **Pathway analysis.** (A) FA synthesis pathways in infected cells demonstrated by comparing the 3hpi to the 2hpi timepoint. **(**B) Active pathways in infected cells as comparing 2hpi to baseline (time 0). Green and red arrows show reactions with positive and negative Z-scores respectively, thus

showing pathways with increased and decreased reactivity. The boxes highlight potential changed
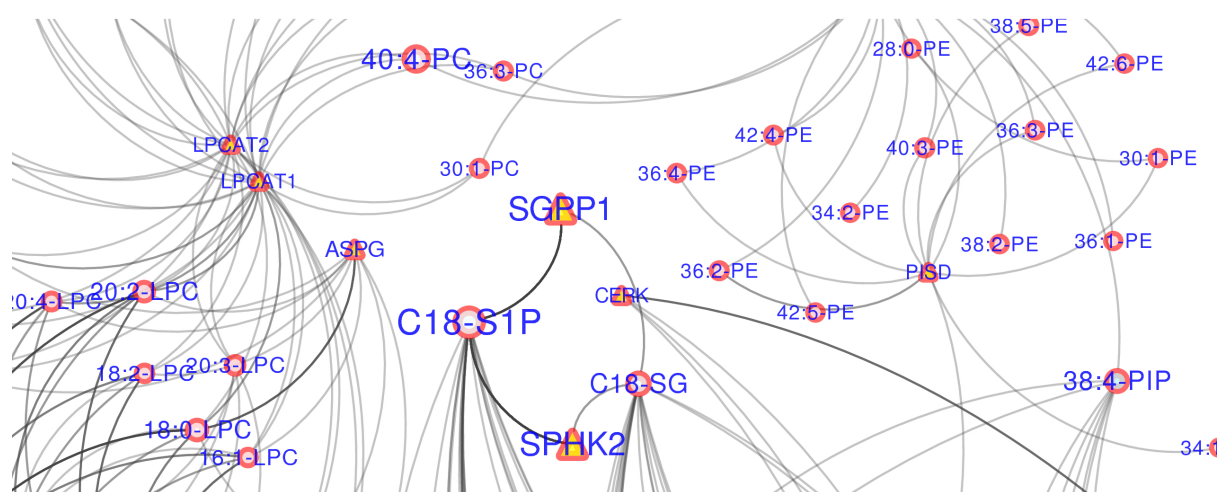
pathways based on Z-scores.

Figure 4. **Optimal subnetwork analysis**. A subsection of the subnetwork analysis performed

comparing the lipid composition at 2hpi with that of uninfected cells. The red and yellow dots are

respectively metabolites and proteins. The thickness of edges is proportional to their robustness
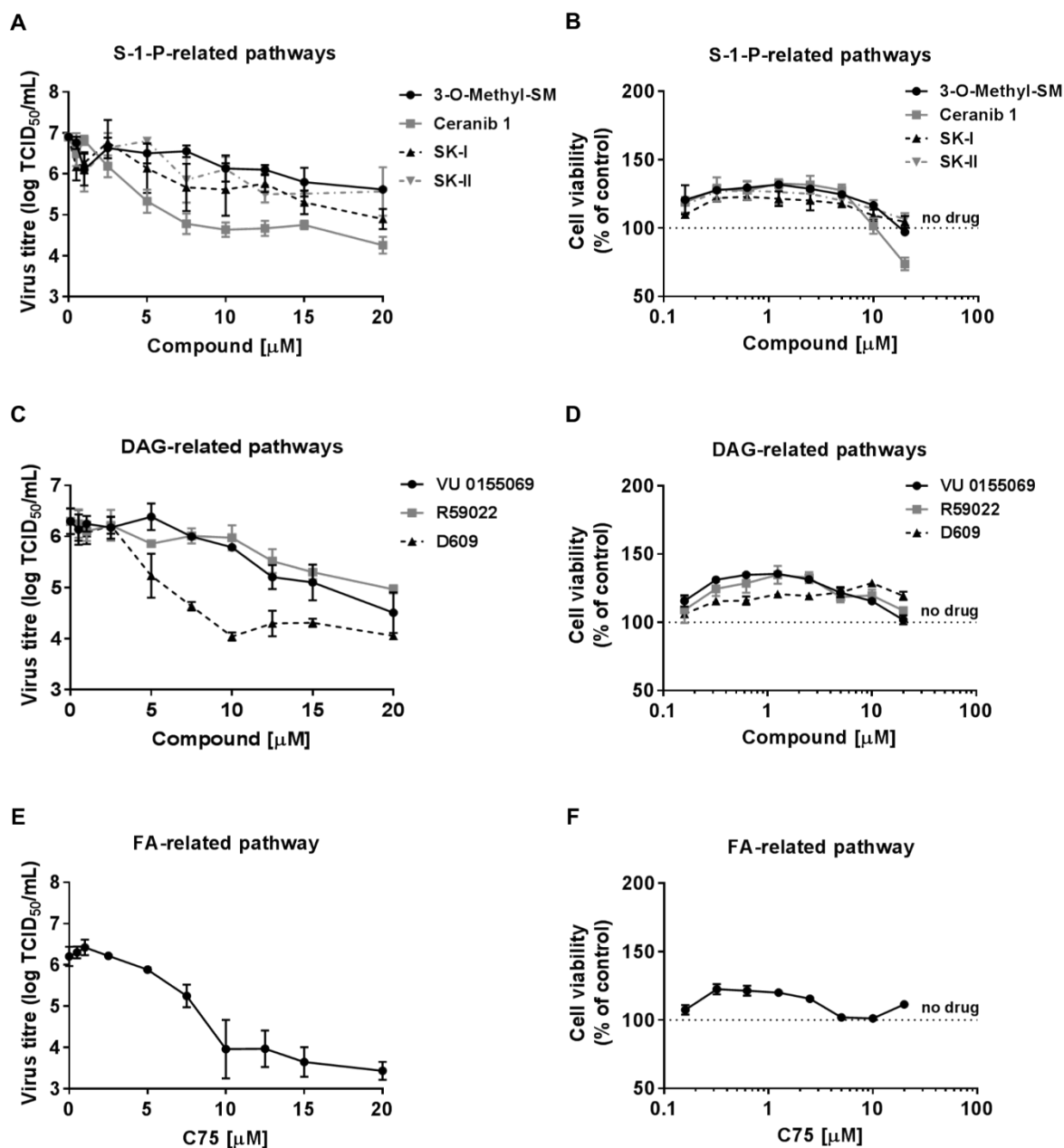
scores.

Figure 5. Quantification of RV-A1b replication inhibition over full drug concentration-response curves.

(A, C, E) HBECs were pre-treated for 1h with increasing concentrations of compounds (0.1-20µM) or DMSO followed by infection with RV-A1b at an MOI of 5 for 1h. Replication proceeded for 7h and cell lysates with supernatants were harvested and processed to measure virus titres by TCID$_{50}$. The graphs show means (± SEM) of three independent repeats each performed in duplicate. Differences between

the range of drug concentrations and DMSO-infected cells were estimated by one-way ANOVA with Dunnet's *post hoc* test. *, P<0.05; **, P<0.01; ***, P<0.001; ****, P<0.0001. (B, D, F) HBECs were incubated with drugs for 9h and cell viability was determined using the ToxGlo assay. The graph shows the % of cell viability compared to the control from three independent experiments. Viability of cells untreated is represented by the dotted line.
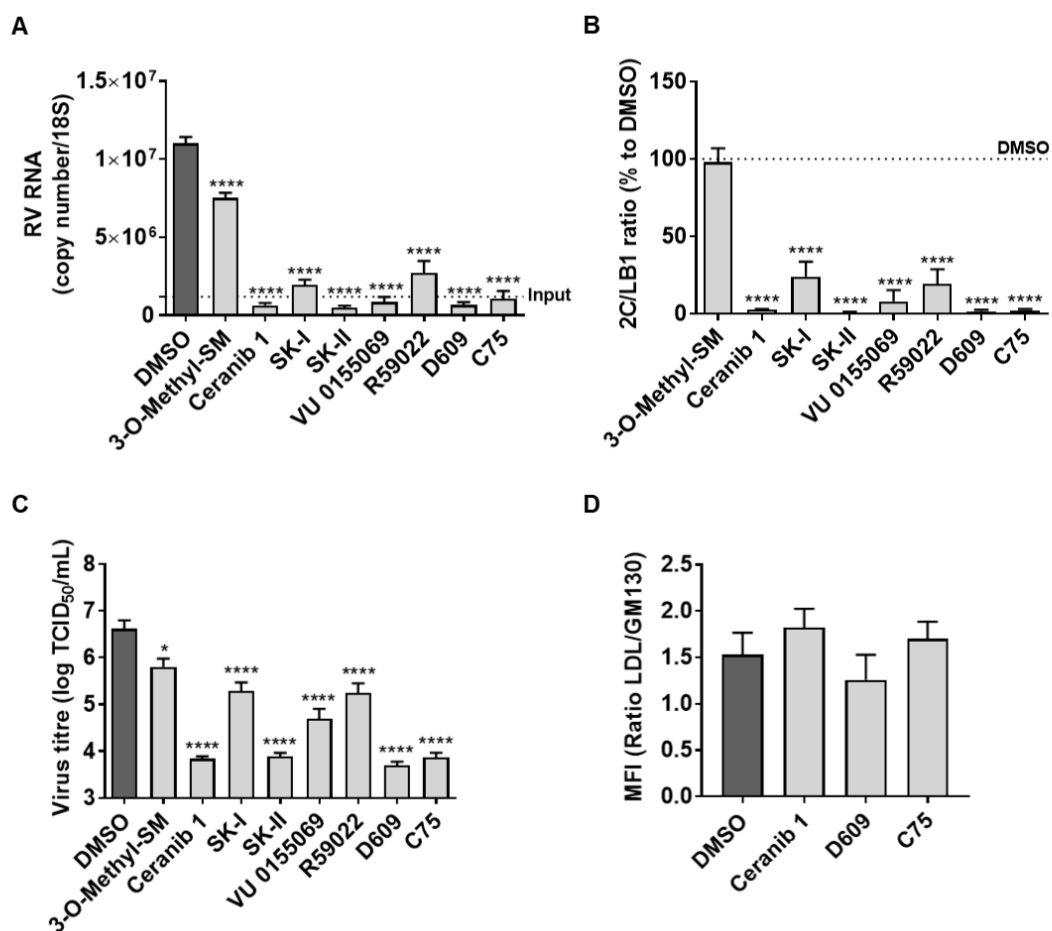
A

B

C

D

Figure 6. Effect on RV genome, protein and titre and LDL uptake.

HBECs pre-treated with a maximal non-cytotoxic concentration (10µM for Ceranib 1 and D609; 20µM for 3-O-Methyl-SM, SK-I, SK-II, VU 0155069 and C75) or DMSO for 1h followed by infection with RV-A1b at an MOI of 5 for 1h. After 7h (A) viral genome replication was measured by qRT-PCR, (B) viral protein synthesis by western blotting and (C) virus titre by $TCID_{50}$. (A) viral RNA levels normalised to 18S rRNA levels in the different conditions. The dotted line represents cell-bound viral RNA at the start of the replication cycle. (B) Western blots were scanned with ImageJ and represented as % of 2C/LB1 ratio over control. (C) Virus titres measured by endpoint titre determination ($TCID_{50}$). (D) BODIPY-non-acetylated LDL uptake in cells pretreated with inhibitors for 1h. Graphs show means ± SEM of three

independent experiments and the differences between DMSO and the different inhibitors estimated

by one-way ANOVA with Dunnet's *post hoc* test. ***, P<0.001; ****, P<0.0001.